

LONG-TERM SPIN STATE ESTIMATION AND PREDICTION FOR DEFUNCT GEO SATELLITES

C. J. Benson and M. J. Holzinger

University of Colorado Boulder, Boulder, Colorado 80303, USA email: conor.j.benson@colorado.edu

ABSTRACT

We present an averaged spin state estimation and prediction framework and apply it to observations of defunct satellites in geosynchronous earth orbit (GEO). This framework averages a uniformly rotating object's attitude dynamics over rotational phase and earth orbit, enabling fast, accurate spin state propagation months or years into the future. By averaging, we distill solar radiation torques to simple curves that are readily modeled as Fourier series. Using just light curve-derived spin rate measurements (although other measurement types can be readily incorporated), we estimate an object's inertial spin rate and spin axis as well as its Fourier solar torque and gravity gradient coefficients in a statistical least squares filter. Inertial spin axis information is provided by torque-driven dynamical coupling between the spin rate and spin axis as well as differences between the inertial and observed spin rate due to time-varying observation geometry. These estimates can be used for long-term (month to year) spin state prediction and updated through catalog maintenance observations. We apply the framework to real light curves of Telstar 401 and compare our estimate to independent Deep Space Network radar solutions, showing clear consistency.

Keywords: averaged attitude dynamics; estimation; light curves.

1. INTRODUCTION

There are currently more than 1000 defunct satellites and rocket bodies near geosynchronous earth orbit (GEO) [17]. This number continues to rise as more satellites are launched and decommissioned. The rotation states of these large, uncontrolled objects can change significantly over time due to solar radiation and thermal re-emission torques as well as gravity gradient torques from earth [1, 8, 5, 7, 6, 9, 10, 18]. For example, the retired GEO weather satellite GOES 8 spun down from ~ 3.5 revolutions per minute (rpm) to nearly zero in less than one year before spinning back up in non-principal axis rotation [8].

The ability understand and predict the natural spin state evolution of defunct satellites and rocket bodies is important for a number of applications. First, object attitude knowledge will increase orbit prediction accuracy through improved modeling of attitude-dependent forces (e.g. solar radiation pressure and atmospheric drag). Second, target attitude knowledge is crucial for active debris removal (ADR) missions to rendezvous with, grapple, and de-spin these large, non-cooperative objects. With the significant observed spin state evolution of many defunct objects, long-term attitude prediction would be valuable to identify favorable windows of slow rotation. This would reduce mission risk and the time and energy required to de-spin an object. Spin state prediction is also important to predict spin-driven material shedding events. It is currently unclear if defunct object spin rates can increase unbounded, ultimately resulting in catastrophic break-up. Even strictly dissipative eddy current torques, which are weak at GEO given their $1/R^6$ fall-off with distance from the earth, do not limit rotation parallel to earth's magnetic field [13]. Improved understanding of spin state evolution across the broad defunct satellite and rocket body population can inform whether spin-driven break-up is possible.

Understanding spin state evolution of defunct satellites will inform decommission procedures to minimize post-disposal spin rates and maximize long-term predictability. For example, differences in the end of life solar array angles and resulting solar torques of the nearly-identical GOES 8-12 satellites have led GOES 8 and 12 to evolve rapidly while GOES 10's uniform spin rate has remained nearly constant [9]. For space traffic management (STM) and space situational awareness (SSA) there is a need to determine whether objects are active or uncontrolled. This can be informed by observed attitude evolution. Unlike orbital dynamics where divergence from a ballistic trajectory indicates control, there is no established ballistic baseline for attitude motion. In other words, we do not fully understand what natural attitude motion of large, defunct objects looks like to formally distinguish natural from controlled motion. Further study of long-term attitude evolution across the defunct object population can inform this ballistic baseline.

A number of studies have been conducted to estimate and predict the attitude motion of well-known defunct satellites (e.g. [14, 15]). These studies generally require de-

tailed knowledge of an object’s properties (shape, moments of inertia, surface materials, etc.). Unfortunately, we lack detailed knowledge of most defunct objects. The attitude dynamics are very sensitive to shape, moments of inertia, body-frame principal axis directions, and optical properties [9, 6, 7]. These studies also generally rely on resolved measurements given the complexities and ambiguities associated with non-resolved light curve inversion, even with high fidelity spacecraft models [8]. Diffraction limits preclude ground-based resolved imagery beyond LEO for all but the largest, adaptive optics-equipped telescopes. Doppler-delay radar measurements require large, powerful antennas due to the $1/R^4$ echo power fall-off with distance, and satellite laser ranging requires targets to have retro-reflectors. We lack sufficient resources to regularly collect resolved measurements for attitude estimation across the broad debris population, especially beyond LEO. Overall, we desire a dynamics-based spin state estimation and prediction approach that relies primarily on readily-obtained non-resolved optical light curves for measurements and minimal a priori information about a particular object for applicability to the broad defunct space object population.

In this work, we present an averaged spin state estimation and prediction framework first discussed in Ref. [2]. We first outline the method which is founded on averaging the slowly-varying equations of motion for a uniformly rotating object’s inertial spin rate and spin axis over the object’s intrinsic rotation and earth orbit. We then explore simulated test cases and apply the approach to real observations of the defunct GEO satellite Telstar 401.

2. METHODS

2.1. Frames

There are several frames to define that simplify the dynamical modeling and estimation. The first is the rotating heliocentric orbit (\mathcal{O}) frame (see Figure 1), centered at the satellite and defined by the \hat{X} , \hat{Y} , and \hat{Z} axes. \hat{Z} points from the satellite to the sun, \hat{X} points along the instantaneous angular velocity of the \mathcal{O} frame with respect to the inertially-fixed \mathcal{N} frame, denoted by $\omega_{\mathcal{O}/\mathcal{N}}$. Here \mathcal{N} is taken to be equatorial earth-centered inertial (ECI) J2000. Finally, \hat{Y} completes the orthogonal basis set. The angular velocity $\omega_{\mathcal{O}/\mathcal{N}}$ is given by,

$$\omega_{\mathcal{O}/\mathcal{N}} = \frac{1}{u} \hat{\mathbf{u}} \times \dot{\hat{\mathbf{u}}} \quad (1)$$

where \mathbf{u} and $\dot{\mathbf{u}}$ are the position vector and inertial velocity of the sun relative to the satellite, $u = |\mathbf{u}|$, and $\hat{\mathbf{u}} = \mathbf{u}/u$. Note that $\hat{\mathbf{u}}$ and \hat{Z} are co-aligned. We neglect the satellite’s geocentric orbit when computing \mathbf{u} and $\dot{\mathbf{u}}$ because variations are negligible for earth-orbiting objects. For example at GEO, the sun direction varies by less than $\sim 0.03^\circ$ from one side of the orbit to the other.

Also, variations in the sun-satellite distance and direction due to the geocentric orbit are averaged out in our upcoming equations. So in practice, \mathbf{u} and $\dot{\mathbf{u}}$ are taken as the earth-sun position and velocity and are computed from NAIF SPICE ephemerides.

Rotation from the \mathcal{O} frame to the \mathcal{N} frame is given by the following matrix,

$$ON = \begin{bmatrix} \mathcal{N}\hat{X}^T \\ \mathcal{N}\hat{Y}^T \\ \mathcal{N}\hat{Z}^T \end{bmatrix} \quad (2)$$

where the superscript \mathcal{N} denotes vectors defined in the \mathcal{N} frame and T is the vector transpose.

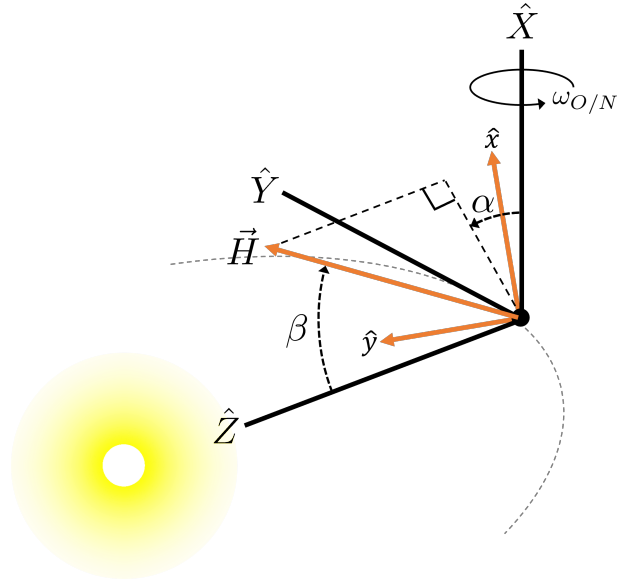


Figure 1: Orbit (\mathcal{O}) and angular momentum (\mathcal{H}) frames, denoted by black and orange vectors respectively.

The second frame shown in Figure 1 is the rotational angular momentum (\mathcal{H}) frame denoted by the \hat{x} , \hat{y} , and \hat{H} axes. \hat{H} (also denoted by \hat{z}) is along the satellite’s rotational angular momentum vector. Rotation from the \mathcal{O} frame to the \mathcal{H} frame is defined by the two angles α and β . These angles are essentially the spherical coordinates of \hat{H} in the \mathcal{O} frame. The clocking angle α defines rotation of \hat{H} around the sun-line and β is the angle between the sun-line and \hat{H} . The unit vector \hat{x} points in the direction of increasing β and \hat{y} (which is orthogonal to the sun-line) in the direction of increasing α . The rotation matrix from the \mathcal{O} to \mathcal{H} frame is given by,

$$HO = R_2(\beta)R_3(\alpha) \quad (3)$$

where $R_i()$ is a rotation about the i th principal axis [19].

2.2. Averaged Attitude Dynamics

In this work we account for solar radiation and gravity gradient torques since these are by far the dominant external perturbations at GEO [13]. For large satellites with

non-negligible spin rates, these torques are small perturbations on the torque-free rotation. Combined with $\omega_{O/N}$ being only $\sim 1^\circ/\text{day}$, the angles α and β as well as the satellite's inertial spin rate $\omega_e = 2\pi/P_e$ change slowly compared to the satellite's rotational phase and geocentric true anomaly. Analogous to the Lagrange and Gauss planetary equations for osculating orbital elements which can be averaged over fast periodic perturbations [22], we average equations of motion for α , β , and ω_e over the satellite's rotation and geocentric orbit. In this work, we assume the satellite is in a uniform (flat) spin with a rotation period non-resonant with the geocentric orbit period.

The resulting spin and orbit-averaged equations of motion for the $\hat{\mathbf{H}}$ clocking and coning angles α and β and the inertial spin rate ω_e are given by [7],

$$\dot{\alpha} = \frac{\tilde{M}_y(\beta) + \tilde{L}_y(\alpha, \beta)}{\omega_e \sin \beta} + \frac{\omega_{O/N} \cos \alpha}{\tan \beta} \quad (4)$$

$$\dot{\beta} = \frac{\tilde{M}_x(\beta) + \tilde{L}_x(\alpha, \beta)}{\omega_e} + \omega_{O/N} \sin \alpha \quad (5)$$

$$\dot{\omega}_e = \tilde{M}_z(\beta) \quad (6)$$

Here \tilde{M}_x , \tilde{M}_y , and \tilde{M}_z are the averaged \mathcal{H} frame solar torque components. For instantaneous thermal re-emission (i.e. no thermal lag), these torques are just functions of satellite properties and β . The tilde denotes that they have been divided by the satellite's maximum moment of inertia I_s which we assume to be unknown. Similarly, \tilde{L}_x and \tilde{L}_y are the averaged gravity gradient torque components in the \mathcal{H} frame. Finally, $\omega_{O/N} = |\omega_{O/N}|$.

The inertia-normalized, spin and orbit-averaged gravity gradient torque is given by [23],

$$\tilde{\mathbf{L}} = \frac{3}{2} \frac{\mu}{a^3(1-e^2)^{\frac{3}{2}}} I_{gg} (\hat{\mathbf{H}} \cdot \hat{\mathbf{H}}_G) (\hat{\mathbf{H}} \times \hat{\mathbf{H}}_G) \quad (7)$$

where a and e are the satellite's geocentric semi-major axis and eccentricity, and $\hat{\mathbf{H}}_G$ is its geocentric orbital angular momentum direction. Finally, $I_{gg} = 1 - I_t/I_s$ is the gravity gradient inertia parameter where $I_t = \frac{1}{2}(I_l + I_i)$ is the average of the minimum and intermediate moments of inertia I_l and I_i . I_{gg} has the physical bounds of 0 for equal inertias (e.g. a sphere) and 0.5 for an extremely thin rod or disk. Since $\tilde{\mathbf{L}}$ is perpendicular to $\hat{\mathbf{H}}$ given the cross-product in Eq. 7, the averaged gravity gradient does not change the satellite spin rate. So, $\tilde{L}_z = 0$. Finally, in \mathcal{H} frame components, $\hat{\mathbf{H}}_G$ is given by,

$${}^{\mathcal{H}}\hat{\mathbf{H}}_G = HOON \begin{bmatrix} \sin \Omega \sin i \\ -\cos \Omega \sin i \\ \cos i \end{bmatrix} \quad (8)$$

where Ω and i are the equatorial J2000 right ascension of the ascending node (RAAN) and inclination of the satellite's geocentric orbit. In this work, we obtain a , e , i , and Ω from two line elements (TLEs) making sure to properly convert the TLE's Kozai mean motion to semi-major axis [12] and transform Ω and i from true equator, mean equinox (TEME) to J2000 [22].

2.3. Solar-Torque Modeling

Spin-averaging enables the use of simple expressions for the solar radiation torque. By averaging over the satellite's rotation, we can boil complex dependencies on the satellite geometry and material reflective properties down to curves that are just a function of β . As an example, we compute the spin-averaged torques for the Optus B3 model provided in Figure 2. The model consists of 928 facets to accurately capture self-shadowing between the bus, solar arrays, and antennae. Assuming instantaneous thermal re-emission, we account for specular and diffuse reflection using the force model provided by McInnes [16]. We also account for material-specific reflective properties for satellite bus multi-layer insulation (MLI), solar cells, graphite solar array back-side, and carbon fiber reinforced antennae. We assume the satellite's center of mass is shifted 10 cm along the solar array axis from the center of the bus and that the principal axes are aligned with the body axes in Figure 2.

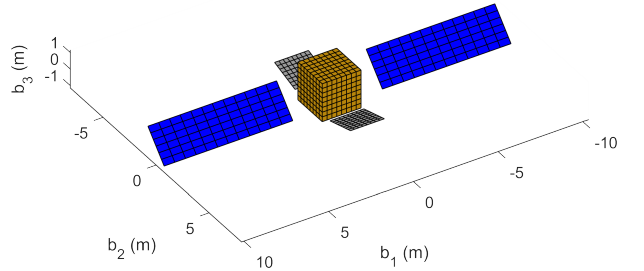


Figure 2: Optus B3 shape model (928 facets)

The resulting spin-averaged \mathcal{H} frame torque components along the maximum inertia (\hat{b}_3) axis are provided in Figure 3. These torques have been normalized with respect to Optus B3's maximum inertia $I_s = 6143 \text{ kg}\cdot\text{m}^2$. The non-smooth nature of \tilde{M}_y , particularly near $\beta \sim 20^\circ$, is due to self-shadowing between the bus and antennae. \tilde{M}_x and \tilde{M}_y are identically zero at $\beta = 0^\circ$ and 180° . This is due to the following. When the sun is along the spin axis, the body frame torques are constant. So when averaged, the torques perpendicular to the spin axis average to zero as they sweep out all possible directions. Also included in Figure 3 are 4th order Fourier series least squares fits to these torques, leveraging the extremal constraints for \tilde{M}_x and \tilde{M}_y [21]. The \tilde{M}_x and \tilde{M}_z fits nearly indistinguishable from the numerical model. Higher order Fourier series will naturally improve the fit.

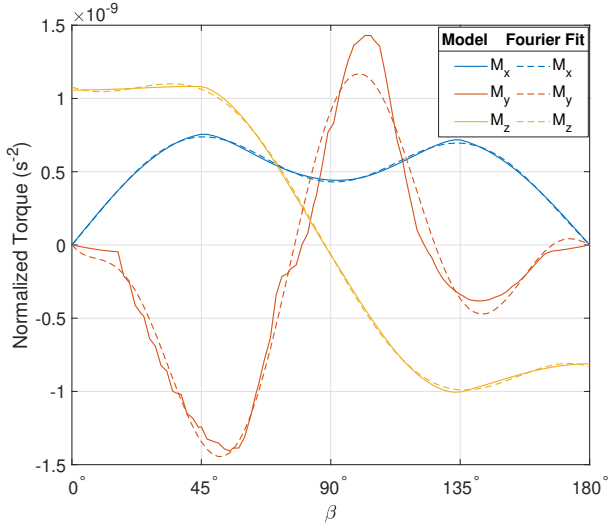


Figure 3: Optus B3 numerically computed spin averaged solar torques and 4th order ($m = 4$) Fourier series fits.

So in this work, we model and estimate the solar torques with Fourier series. With ${}^{\mathcal{H}}\underline{\tilde{M}}(\beta) = [\tilde{M}_x, \tilde{M}_y, \tilde{M}_z]^T$, the Fourier torques are,

$${}^{\mathcal{H}}\underline{\tilde{M}}(\beta) = \frac{d_{AU}^2}{u^2} \left\{ \underline{c}_0 + \sum_{n=1}^m \left[\underline{a}_n \cos(n\beta) + \underline{b}_n \sin(n\beta) \right] \right\} \quad (9)$$

where \underline{c}_0 , \underline{a}_n , and \underline{b}_n are the 3×1 Fourier coefficient vectors corresponding to a distance of d_{AU} (149.6×10^{-6} km), m is the Fourier order, and d_{AU}^2/u^2 accounts for the varying sun-satellite distance due to earth's eccentricity.

The four constraints for \tilde{M}_x and \tilde{M}_y are given by,

$$\begin{aligned} \tilde{M}_x(0^\circ) &= c_{x_0} + a_{x_1} + a_{x_2} + a_{x_3} + \dots = 0 \\ \tilde{M}_x(180^\circ) &= c_{x_0} - a_{x_1} + a_{x_2} - a_{x_3} + \dots = 0 \\ \tilde{M}_y(0^\circ) &= c_{y_0} + a_{y_1} + a_{y_2} + a_{y_3} + \dots = 0 \\ \tilde{M}_y(180^\circ) &= c_{y_0} - a_{y_1} + a_{y_2} - a_{y_3} + \dots = 0 \end{aligned} \quad (10)$$

2.4. Measurement Model

For non-resolved light curves, a satellite's measured (synodic) spin rate ω_s will differ from the inertial spin rate ω_e due to motion of the phase angle bisector (PAB) [11]. The PAB, denoted by \hat{p} , lies halfway between the satellite-sun direction \hat{u} and satellite-observer direction \hat{o} ,

$$\hat{p} = \frac{\hat{u} + \hat{o}}{|\hat{u} + \hat{o}|} \quad (11)$$

The observed spin rate ω_s is then related to ω_e by,

$$\omega_s = \omega_e - \dot{\lambda}(\alpha, \beta) \quad (12)$$

where $\dot{\lambda}$ is the longitude rate of \hat{p} relative to the satellite spin axis. When observing objects with spin rates much faster than their orbital motion, the PAB moves primarily in body frame longitude. Therefore, over relatively short timescales (a handful of object rotations), longitudinal reflective features dominate the light curve frequency structure. So it is this longitude component of PAB motion that primarily drives differences between ω_e and ω_s . We desire an analytical solution for $\dot{\lambda}$ to facilitate partial derivative computation in our estimation framework.

The inertial time derivative of \hat{p} is given by,

$$\dot{\hat{p}} = \frac{1}{|\hat{u} + \hat{o}|} \left[\dot{\hat{u}} + \dot{\hat{o}} - \hat{p} \left\{ (\dot{\hat{u}} + \dot{\hat{o}}) \cdot \hat{p} \right\} \right] \quad (13)$$

where the unit vector time derivatives $\dot{\hat{u}}$ and $\dot{\hat{o}}$ can be computed using the same functional form below,

$$\dot{\hat{s}} = \frac{1}{s} \left[\dot{\underline{s}} - \hat{s} (\dot{\underline{s}} \cdot \hat{s}) \right] \quad (14)$$

Denoting \hat{t} as the direction of increasing satellite body-frame longitude,

$$\hat{t} = \frac{\hat{H} \times \hat{p}}{|\hat{H} \times \hat{p}|} \quad (15)$$

with $\sin \phi = |\hat{H} \times \hat{p}|$, the PAB longitude rate $\dot{\lambda}$ is then,

$$\dot{\lambda}(\alpha, \beta) = \frac{\dot{\hat{p}} \cdot \hat{t}}{\sin \phi} \quad (16)$$

We see that $\dot{\lambda}$ will increase as the angle ϕ between \hat{p} and \hat{H} decreases. At higher body-frame latitudes, longitude lines converge, so \hat{p} will move faster in longitude near the poles than at the body's equator.

Figure 4 shows synodic period variations at GEO for several inertially-fixed spin pole latitudes. For clarity, the synodic period is only plotted for phase angles $\theta = \cos^{-1}(\hat{u} \cdot \hat{o})$ less than 60° corresponding to night-time observation. The satellite has an inertial rotation period (P_e) of 160 s and an orbital inclination of 15° . For 60° and 90° pole latitudes, the spin axis is mostly perpendicular to the PAB for an earth-based observer, so the synodic period is relatively constant over the year. As the pole latitude decreases towards the orbit plane, there are portions of the year where the PAB moves close to the spin axis, resulting in nightly variations of almost 1 s. Such variations are readily detectable in dense, high quality, light curve observations. Synodic period variations increase with slower inertial rotation. Also, the Figure 4 results are for prograde rotation (i.e. positive pole latitude). For retrograde rotation (i.e. negative pole latitudes), the Figure 4 prograde solutions will essentially be reflected across the 160 s line (i.e. the synodic period will generally be lower than the inertial period). Sensitivity of the synodic period to the inertial spin pole direction demonstrates the utility of leveraging synodic variations for spin pole estimation.

Furthermore, changes in ω_s due to inertial acceleration from external torques will be superimposed on the nightly synodic variation.

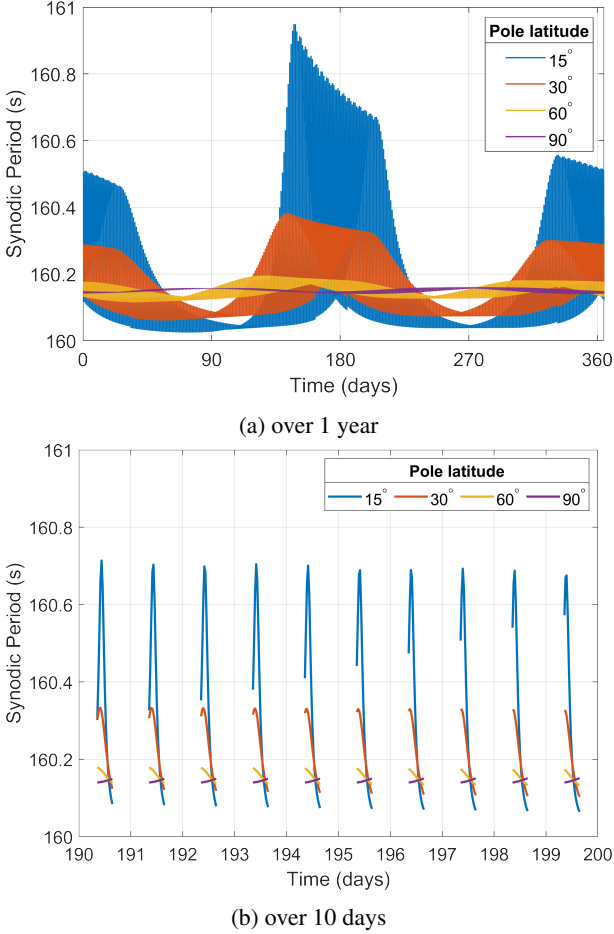


Figure 4: Variations in the synodic period of a GEO satellite for an earth-based observer ($P_e = 160$ s)

2.5. Estimation Framework

We can now discuss the spin state estimation framework. Our state vector consists of the following components,

$$\underline{\mathbf{X}} = [\alpha \ \beta \ \omega_e \ \underline{\mathbf{c}}_0^T \ \underline{\mathbf{a}}^T \ \underline{\mathbf{b}}^T \ I_{gg}]^T \quad (17)$$

with dynamics given by,

$$F(\underline{\mathbf{X}}) = [\dot{\alpha} \ \dot{\beta} \ \dot{\omega}_e \ \mathbf{0}_{1 \times n_c}]^T \quad (18)$$

where n_c is the total number of Fourier and gravity gradient coefficients, all assumed to be constant. In this work, we assume that our measurements are synodic spin rates obtained from light curve frequency analysis.

$$G(\underline{\mathbf{X}}) = \omega_s = \omega_e - \dot{\lambda}(\alpha, \beta) \quad (19)$$

Other measurement types can be readily incorporated. These include direct inertial spin pole measurements as

well as indirect measurements like Doppler bandwidth which provides the angle between the spin axis and radar line of sight [4, 5].

Finally, we have the four constraints on the \tilde{M}_x and \tilde{M}_y Fourier coefficients given by Eq. 10 which can be written more compactly in the following form,

$$[C]\underline{\mathbf{X}} = \underline{\mathbf{b}} = \mathbf{0}_{4 \times 1} \quad (20)$$

We use a statistical least squares (batch) estimator [20] to fit our state $\underline{\mathbf{X}}$ at a specific epoch to the measurements $G(\underline{\mathbf{X}})$ using the Eq. 20 constraints [21].

3. SIMULATION RESULTS

We will now explore the spin state estimation framework for a simulated test case. The TLE ephemerides for the defunct GEO satellite EchoStar 2 are used to compute observation geometry and the geocentric orbital elements. The initial simulation epoch is January 1, 2022 00:00 UTC. Synodic spin rate measurements are taken from Flagstaff, Arizona, USA (35.1846° N, 111.7444° W, 2270 m elevation). After the first 4 nights where 3 - 6 hours of obs are taken with a 30 minute measurement cadence, a single synodic measurement is taken every 7 - 16 days for one year. Observations are only taken at phase angles less than 45° to simulate night-time observation.

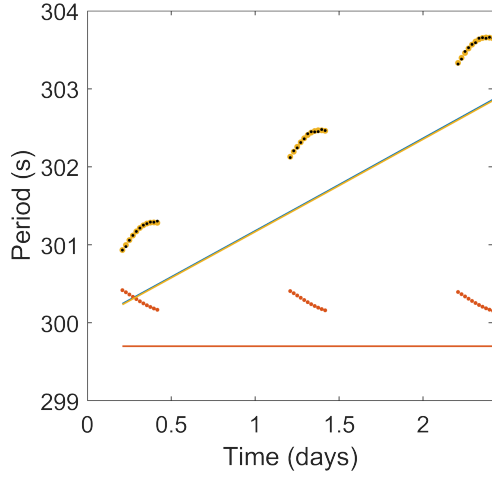
The truth state is: $\alpha_0 = 0^\circ$, $\beta_0 = 150^\circ$, $P_e = 300$ s, $I_{gg} = 0.396$. We assume the numerically computed Optus B3 solar torques from Figure 3 as truth, evaluating them with interpolated lookup tables. We propagate these truth dynamics forward and generate simulated synodic spin rate observations.

The a priori spin period estimate is $P_e = 299.7$ s with $I_{gg} = 0.45$. Since we generally lack a priori spin axis information, we generate 24 hypotheses for the initial spin pole direction with α ranging from 0° to 315° and β from 45° to 135°, both in 45° increments. For reference to the resulting estimates, the hypotheses are numbered in terms of increasing α first. We model \tilde{M}_x , \tilde{M}_y , and \tilde{M}_z as 6th order Fourier series and set all a priori coefficient values to zero. Therefore, we make no assumptions about the solar torque structure.

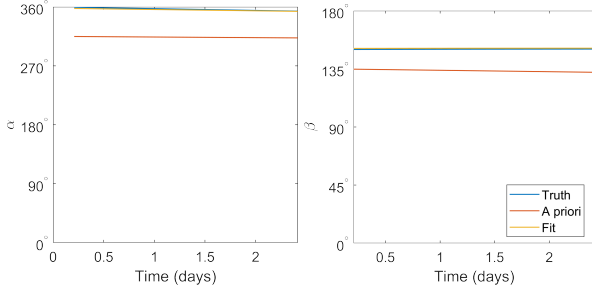
For numerical stability in the batch filter, we scale up the small solar torque coefficients for commensurability with α , β , ω_e , and I_{gg} and scale the simulation time accordingly. For a priori covariance \bar{P}_0 in the filter [20], we assume 1- σ uncertainties of 3° for α and β , 0.1 for the scaled Fourier coefficients, 0.1 rad/s for ω_e , and 0.03 for I_{gg} . A 0.01 s 1- σ uncertainty is applied as random noise to the true synodic period measurements.

Starting at the initial epoch, we fit each hypothesis to increasing timespans of measurements, saving the updated estimates as new a priori and refitting over a larger fraction of the data. During this process, if β leaves (0°,

180°), I_{gg} exceeds physical bounds, the satellite spin rate reaches zero during propagation, or the post-fit measurement residuals diverge, we attempt to re-fit over shorter and shorter segments until passing these checks. If we cannot add another measurement without failing these checks, we discard the hypothesis. Otherwise, we continue fitting over longer and longer segments until all measurements have been incorporated. These checks solely enforce consistency with the assumed dynamics model and measurements and make no additional assumptions about the object.



(a) dots are synodic periods, solid lines are inertial

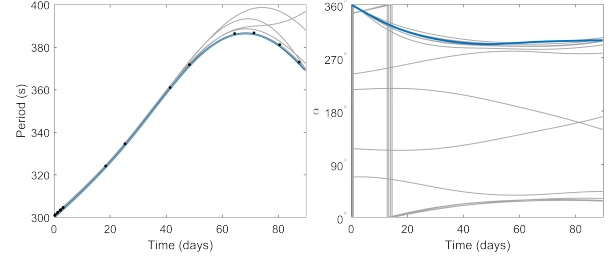


(b) \hat{H} clocking angle α

(c) \hat{H} coning angle β

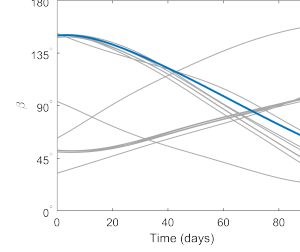
Figure 5: Fit for hypothesis 24 after 3 days (blue is truth)

Figure 5 shows the fitting process for hypothesis 24 ($\alpha_0 = 315^\circ$, $\beta_0 = 135^\circ$) over the first three nights of observations. The blue line in Figure 5a is the true inertial spin period P_e and the black dots are the corresponding synodic measurements with noise added. We can see that the nightly synodic variation is superimposed on the solar torque-driven inertial period change. The initial a priori estimate for hypothesis 24 is shown in red (solid line for P_e , dots for $P_s = 2\pi/\omega_s$). The a priori P_e is constant since we assume zero solar torque a priori. The a priori synodic variation is inconsistent with the measurements due to the initial spin axis being 30.4° from the true location. Minimizing the least squares difference between the predicted and observed measurements, the filter updates the state to the yellow fit which closely overlays the true α , β , and P_e .



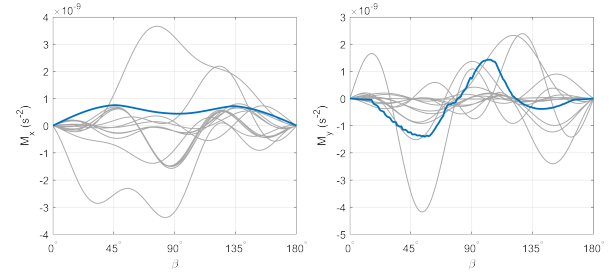
(a) Inertial period (synodic measurements are black dots)

(b) clocking angle α



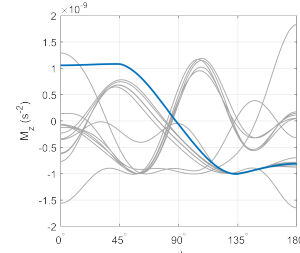
(c) coning angle β

Figure 6: Spin state evolution for all viable hypotheses after 90 days (blue is truth)



(a) \tilde{M}_x

(b) \tilde{M}_y

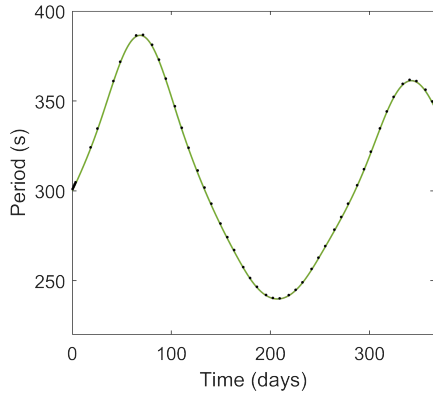


(c) \tilde{M}_z

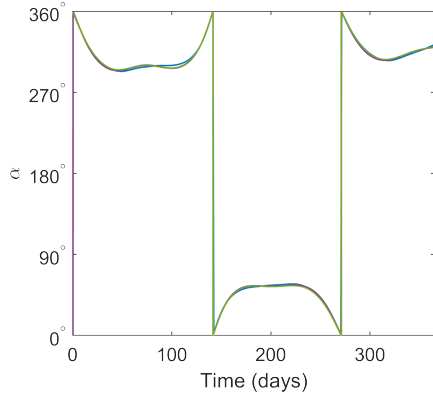
Figure 7: Torque estimates for the all viable hypotheses after 90 days (blue is truth)

Moving out further in time, Figure 6 shows all viable hypotheses after 90 days (with the blue lines denoting the truth). At this point, 11 of the 24 hypotheses have been discarded for failing to pass the above checks. Most of the remaining viable hypotheses are closely tracking the spin period measurements. However, from the α and β estimates we see that the pole solutions fall largely into two groups, the first near the true spin axis and the second attracted to another spin axis that was a well-fitting

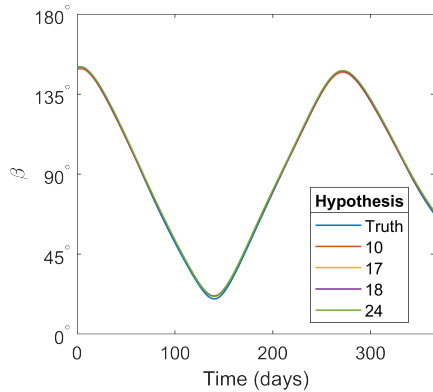
solution to the first 4 nights of dense synodic measurements. We see similar separation in the Figure 7 torque estimates, most notably for \tilde{M}_z where there are two "mirrored" groups of solutions. Overall, we can see several of the torque estimates beginning to converge on the true curves.



(a) Inertial period (synodic measurements are black dots)

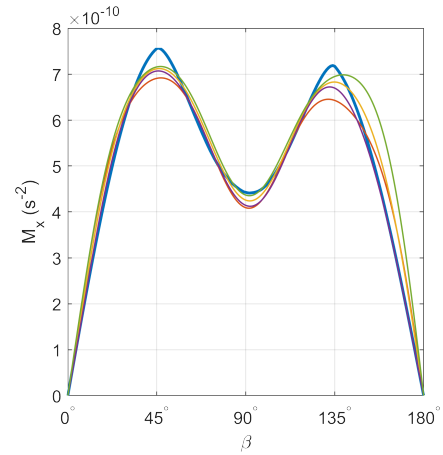


(b) \hat{H} clocking angle α

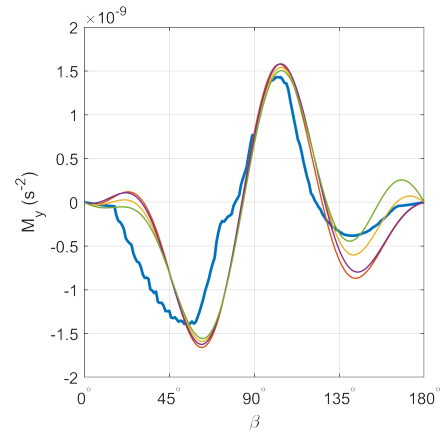


(c) \hat{H} coning angle β

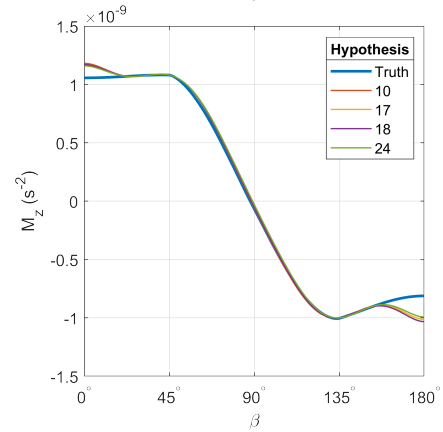
Figure 8: 1 year spin state evolution for the 4 viable hypotheses



(a) \tilde{M}_x



(b) \tilde{M}_y



(c) \tilde{M}_z

Figure 9: 1 year torque estimates for the 4 viable hypotheses

Figures 8 and 9 show the 4 remaining viable hypotheses after 1 year. All other hypotheses have been discarded after failing to pass one or more of the above checks for dynamical and measurement consistency. All 4 estimates closely track the true spin period and pole evolution with torque estimates converging on the true curves. Estimated gravity gradient parameters \hat{I}_{gg} for the 4 hy-

potheses range from 0.360 - 0.384 compared to the true value of 0.396 (3 - 9% difference), due in part to I_{gg} absorbing discrepancies between the true numerical solar torques and truncated Fourier series model. Further observations will improve the torque coefficient and I_{gg} estimates. Also, measurements of the nightly synodic period variation accelerate convergence by providing direct spin axis information. Otherwise, spin axis information is obtained through weaker dynamical coupling between ω_e and the spin axis via the solar torque components.

4. REAL OBSERVATION RESULTS

We will now apply the spin state estimation and prediction framework to real observations of defunct GEO satellites. Data was collected from 2012 - 2018 at two observing sites. The first, affiliated with the Royal Military College of Canada (RMC), is in Greater Napanee, Ontario, Canada (44.1231° N, 76.8903° W, 79 m elevation). The RMC data were collected at a ~ 3.3 second cadence with a 0.28 m telescope and calibrated to apparent magnitudes. Further details on the RMC data collection and reduction can be found in Ref. [10]. The second site is at the United States Naval Observatory (USNO) in Flagstaff, Arizona, USA (35.1846° N, 111.7444° W, 2270 m elevation). The USNO data were collected at a ~ 37 s cadence and calibrated to apparent magnitudes.

To extract synodic spin rate information, we fit each light curve with a model function consisting of a polynomial in time and a Fourier series [11]. The polynomial captures secular changes in the mean magnitude due to varying observation geometry and the Fourier series models the satellite's rotation. A quadratic polynomial and 16th order Fourier series were used in this work. Candidate periods were tested over a range of values obtained from initial inspection. An iterative approach was taken to more finely sample around the best-fit until the relative change in the spin rate estimate dropped below $1e-6$. Visual inspection, minimum dispersion phase-folding, Lomb-Scargle analysis, and consistency with the spin rate trend from nearby light curves was used to disambiguate harmonics, for example the true spin rate and twice the true rate. The midpoint of each light curve was taken as the measurement epoch. Observation arcs spanned ~ 30 minutes to several hours, with a minimum timespan of several rotation periods for measurements to be considered. These synodic spin rate measurements were then processed in the spin state estimation framework.

4.1. Telstar 401

Telstar 401 is a defunct GEO satellite that launched in 1993 and failed on orbit in 1997. As a result, it was never raised to the GEO graveyard and currently librates around the western stable GEO point, making it visible from North America year-round. Figure 10 shows a segment of the Telstar 401 light curve collected at RMC on

June 14, 2012 with the quadratic polynomial + 16th order Fourier series yielding a best-fit period of 161.51 s.

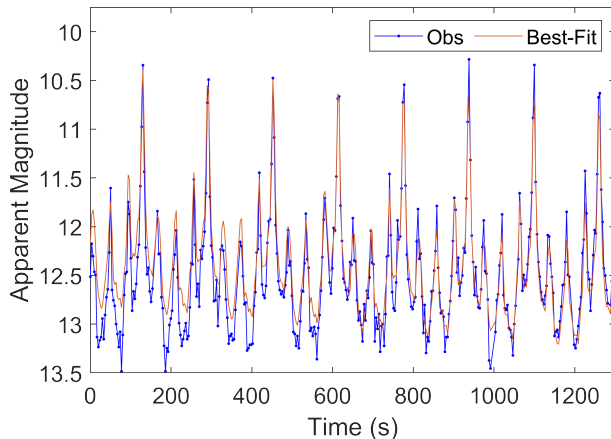


Figure 10: Segment of Telstar 401 light curve on June 14, 2012 with best-fit synodic period estimate (161.51 s)

Figure 11 shows the measured synodic spin period time history for Telstar 401 obtained from RMC and USNO photometry, spanning 5.5 years. Over this timespan, the mean synodic period was ~ 160 s and we see a cyclic period trend similar to that for the simulated case in Figure 8.

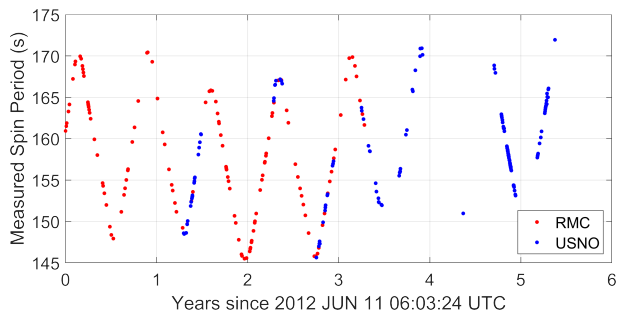


Figure 11: Telstar 401 measured synodic period history

We apply the batch filter to the Figure 11 measurements with a 6th order Fourier series for the solar torques (setting all a priori coefficient values to zero) and assume an a priori I_{gg} of 0.4. We take the synodic measurement on the first night as the a priori inertial period. We consider 264 pole hypotheses with α from 0° to 345° and β from 15° to 165° , both in 15° increments. We assume $1-\sigma$ uncertainties on the angles of 6° .

Processing the observations for each hypothesis using the aforementioned checks, the 7 converged solutions for the inertial period P_e and orbit frame spin axis angles α and β are provided in Figure 12. The synodic period measurements are plotted as black dots. We see the 7 solutions lie nearly on top of each other and all closely track the measured periods.

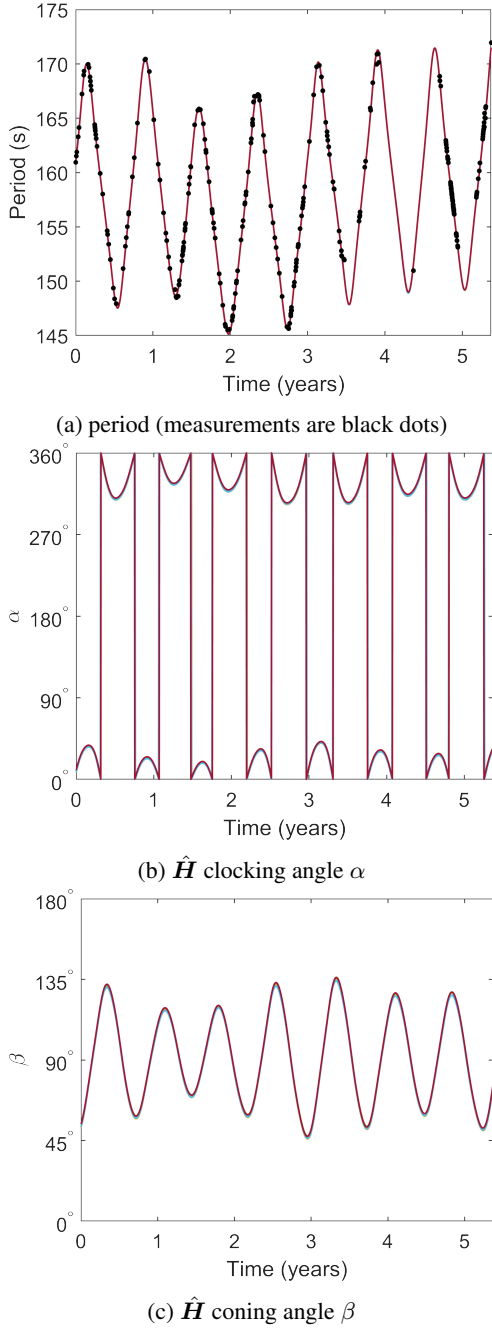


Figure 12: Telstar 401 spin state evolution for the 7 best-fit hypotheses

The corresponding 6th order Fourier series torque estimates are provided in Figure 13. The estimated torques are similar in magnitude to the simulated torques for Opus B3 in Figure 3 with \tilde{M}_x sharing a similar shape. Like the simulated torques, \tilde{M}_z changes sign around $\beta = 90^\circ$ corresponding to Telstar 401's equatorial plane. This \tilde{M}_z sign change, coupled with β variation, drives the cyclic pattern in Telstar 401's synodic spin rate. We should note that the Telstar 401 \tilde{M}_z estimate is largely unconstrained for β values outside $[45^\circ 135^\circ]$ because β never exceeds this range in Figure 12c. So \tilde{M}_z values outside these

bounds are poorly informed. We see a similar behavior in Figure 9c. Torque estimates at these extremal β values would improve if further spin rate measurements are taken when β reaches these values.

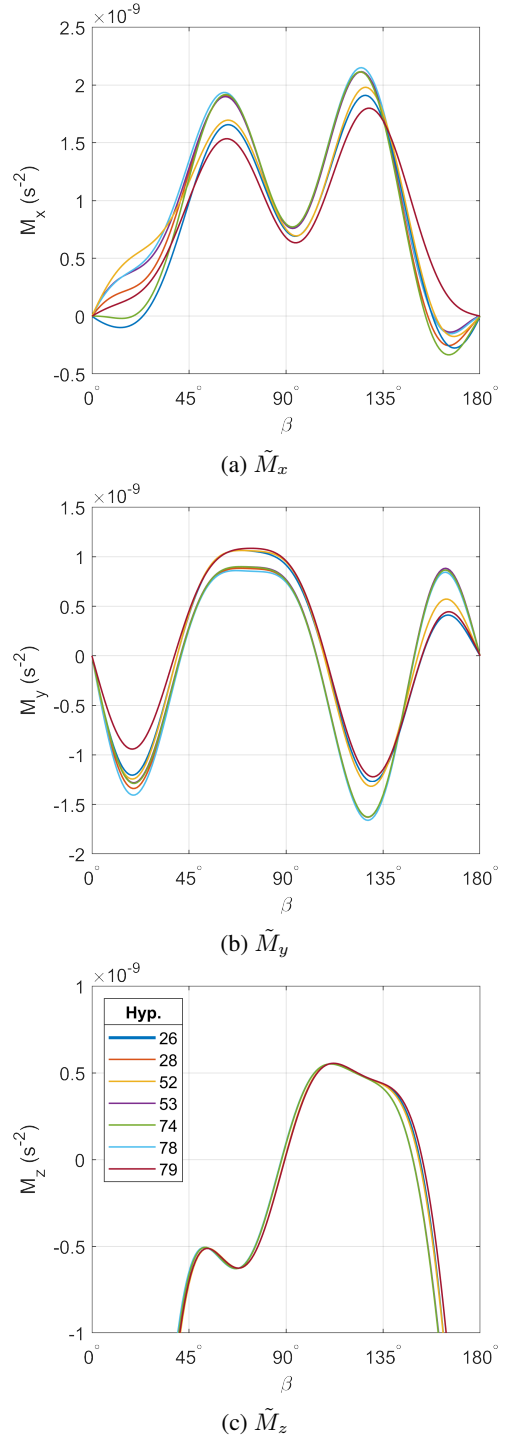


Figure 13: Telstar 401 6th order Fourier series torque estimates for the 7 best-fit hypotheses

To better understand the spin axis evolution of these converged solutions (which are all within several degrees of

each other), Figure 14 shows the hypothesis 26 spin axis time history in equatorial J2000 starting at the green dot on June 11, 2012. Telstar 401’s geocentric orbit normal at the midpoint of the 5.5 year span is given by the dashed line. We can see that Telstar 401’s spin axis precesses clock-wise around the orbit normal direction due to gravity gradient torques which are of similar magnitude to the solar torques.

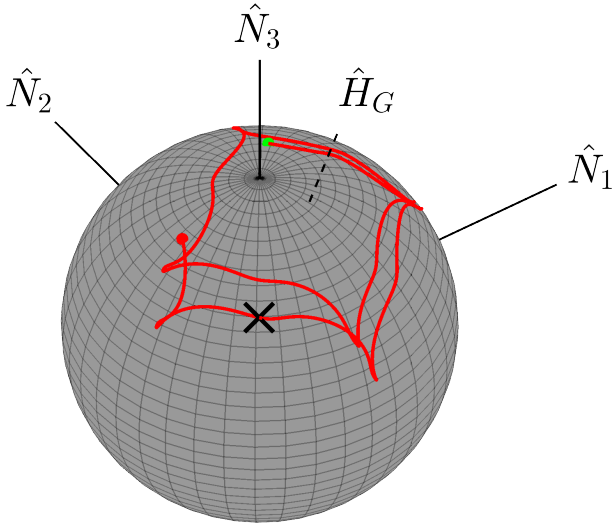


Figure 14: Telstar 401 best-fit spin axis evolution from June 11, 2012 - October 25, 2017 in equatorial J2000 (× denotes the February 27, 2017 location)

The × marker in Figure 14 denotes the estimated pole location on February, 27, 2017. Doppler measurements of Telstar 401 were collected using the Deep Space Network radar antennas in Goldstone, California from late February through early March 2017 [3]. Figure 15 shows the possible radar-derived solutions for Telstar 401’s spin axis over these days. At each epoch, the spin axis lies on one of the corresponding curves [3, 4]. Provided the inertial spin axis does not move, viable spin axis solutions are at the intersection of the curves for all five epochs shown. Our estimate indicates a $\sim 3.2^\circ$ increase in J2000 right ascension (RA) and $\sim 0.5^\circ$ increase in declination (dec) from February 23 - Mar 2, 2017, so the radar-derived spin axis curves may not line up exactly. The dashed circles denote the approximate viable pole regions. The (RA, dec) prediction from our current attitude estimation framework on February 27, 2017 is 235.2° and 44.7° and is marked as shown. This is $\sim 7^\circ$ from the center of the right radar-derived pole region.

Table 1 shows the Telstar 401 hypothesis 26 spin state propagated to the last measurement epoch on October 25, 2017. We note that the best-fit I_{gg} is well-within the viable bounds and suggests a slightly more compact mass distribution than the Optus B3 model ($I_{gg} = 0.396$). Follow-on observations would help further refine this gravity gradient estimate and the solar torque components.

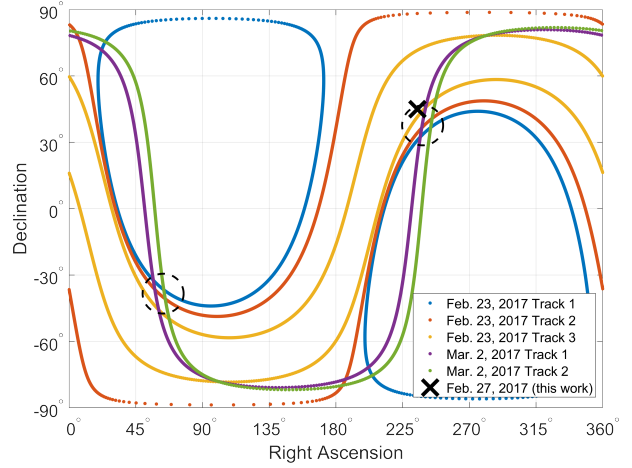


Figure 15: Telstar 401 Deep Space Network radar spin axis solutions and the prediction from this work (equatorial J2000).

Table 1: Telstar 401 best-fit solution on October 25, 2017

\hat{P}_e	$\hat{\alpha}$	$\hat{\beta}$	RA _{J2000}	Dec _{J2000}	\hat{I}_{gg}
171.5 s	32.9°	75.1°	184.3°	60.3°	0.300

5. CONCLUSIONS

We presented an averaged spin state estimation and prediction framework for uncontrolled satellites and rocket bodies. Averaging enables rapid spin state propagation months or years into future. More importantly, by averaging the perturbing torques over the fast angles (object rotational phase and geocentric orbit true anomaly), we distill the torque models to simple curves that we approximate with Fourier series. This enables us to estimate a uniformly rotating object’s spin state and perturbing torques from light curve-derived synodic spin rate measurements with no a priori information. Dynamical coupling between the spin rate and spin axis allows us to tie together long-term observations, strongly constraining viable states. We applied this framework to real observations of the defunct Telstar 401 satellite in GEO and showed close agreement of our estimated spin axis with independent radar-derived measurements. Given the “shape-model free” nature of this approach, it can be readily applied to long-term observations of the broad defunct satellite and rocket body population in GEO and elsewhere.

ACKNOWLEDGMENTS

This work was supported by a United States Air Force Office of Scientific Research (AFOSR) grant (FA9550-23-1-0726). The primary author would like to thank Michael

Earl and Gregg Wade for providing Telstar 401 observations as well as Andrew Edwards for providing the Optus B3 information. The primary author would also like to thank Prof. Dan Scheeres and Dave Monet for their long-term support and encouragement of this research.

REFERENCES

1. A. A. Albuja, D. J. Scheeres, and J. W. McMahon. Evolution of angular velocity for defunct satellites as a result of YORP: An initial study. *Advances in Space Research*, 56(2):237–251, 2015.
2. C. J. Benson. Averaged spin state catalog for uncontrolled space objects. *AAS/AIAA Astrodynamics Specialist Conference, Broomfield, CO*, 2024.
3. C. J. Benson, C. J. Naudet, and Stephen T. Lowe. Radar study of inactive geosynchronous earth orbit satellite spin states (ipn 42-222). *NASA Jet Propulsion Laboratory Interplanetary Network (IPN) Progress Report*, 2020.
4. C. J. Benson, C. J. Naudet, D. J. Scheeres, et al. Radar and optical study of defunct geo satellites. *Proceedings of the Advanced Maui Optical and Space Surveillance Technologies Conference, Maui, HI*, 2020.
5. C. J. Benson, C. J. Naudet, D. J. Scheeres, et al. Radar-derived spin states of defunct geo satellites and rocket bodies. *Proceedings of the Advanced Maui Optical and Space Surveillance Technologies Conference, Maui, HI*, 2021.
6. C. J. Benson and D. J. Scheeres. Averaged solar torque rotational dynamics for defunct satellites. *Journal of Guidance, Control, and Dynamics*, 44(4), 2021.
7. C. J. Benson and D. J. Scheeres. General tumbling-averaged rotational dynamics for defunct satellites. *Journal of Guidance, Control, and Dynamics*, 2022.
8. C. J. Benson, D. J. Scheeres, W. H. Ryan, and E. V. Ryan. Cyclic complex spin state evolution of defunct GEO satellites. *Proceedings of the Advanced Maui Optical and Space Surveillance Technologies Conference, Maui, HI*, 2018.
9. C. J. Benson, D. J. Scheeres, W. H. Ryan, E. V. Ryan, and N. A. Moskovitz. GOES Spin State Diversity and the Implications for GEO Debris Mitigation. *Acta Astronautica*, 167:212–221, 2020.
10. M. A. Earl and G. A. Wade. Observations of the Spin-Period Variation of Inactive Box-Wing Geosynchronous Satellites. *Journal of Spacecraft and Rockets*, 52(3):968–977, 2015.
11. D. Hall, J. Africano, D Archambeault, B. Birge, D. Witte, and P. Kervin. AMOS Observations of NASA’s IMAGE Satellite. *Proceedings of the Advanced Maui Optical and Space Surveillance Technologies Conference, Maui, HI*, 2006.
12. F. R. Hoots, P. W. Schumacher Jr., and R. A. Glover. History of analytical orbit modeling in the U.S. space surveillance system. *Journal of Guidance, Control, and Dynamics*, 27(2), 2004.
13. P. C. Hughes. *Spacecraft Attitude Dynamics*. Dover Publications, New York, NY, 2004.
14. D. Kucharski, G. Kirchner, et al. Photon pressure force on space debris topex/poseidon measured by satellite laser ranging. *Earth and Space Science*, 4, 2017.
15. T. Lips et al. Debris attitude motion measurements and modeling – observation vs. simulation. *Proceedings of the 18th AMOS Conference*, 2017.
16. C. R. McInnes. *Solar Sailing: Technology, Dynamics and Mission Applications*. Springer-Praxis, Chichester, UK, 1st edition, 1999, ch. 2.
17. ESA Space Debris Office. ESA’s annual space environment report (issue 7.1). *European Space Agency*, 2023.
18. A. Rachman, T. Schildknecht, and A. Vananti. Analysis of temporal evolution of debris objects’ rotation rates inside AIUB light curve database (iac-18-a6.3). *Proceedings of the 69th International Astronautical Congress, Bremen, Germany*, 2018.
19. H. Schaub and J. L. Junkins. *Analytical Mechanics of Space Systems*. American Institute of Aeronautics and Astronautics, 3rd edition, 2014, pp. 11, 86-89, 110.
20. B. D. Tapley, B. E. Schutz, and G. H. Born. *Statistical Orbit Determination*. Elsevier Academic Press, 2004.
21. S. Ungalara, E. Dolence, and K. Li. Constrained extended kalman filter for nonlinear state estimation. *8th International IFAC Symposium on Dynamics and Control of Process Systems, Cancun, Mexico*, 2007.
22. D. A. Vallado and W. D. McClain. *Fundamentals of Astrodynamics and Applications*. Microcosm Press, Hawthorne, CA, 4th edition, 2013, Chs. 2, 9.
23. T. Williams, S. Shulman, J. Sedlak, N. Ottenstein, and B. Lounsbury. Magnetospheric multiscale mission attitude dynamics: Observations from flight data. *AIAA/AAS Astrodynamics Specialist Conference, Long Beach, CA*, 2016.